Applied Thermal Engineering 166 (2020) 114648

Contents lists available at ScienceDirect

Applied Thermal Engineering

journal homepage: www.elsevier.com/locate/apthermeng

Research Paper

Experimental and simulation study on thermal characteristics of 18,650 lithium–iron–phosphate battery with and without spot–welding tabs

Shuaihua Liu[a], Xunliang Liu[a,*], Ruifeng Dou[a], Wenning Zhou[a], Zhi Wen[a], Lin Liu[b]

[a] School of Energy and Environmental Engineering, University of Science and Technology Beijing, Beijing 100083, China
[b] Department of Mechanical Engineering, The University of Kansas, Lawrence, KS 66045, USA

HIGHLIGHTS

- The effects of spot-welded nickel strip on battery performance are studied experimentally.
- The effects of ambient temperature on internal heat generation of 18,650 LPF is analyzed.
- A two-dimensional electrochemical–thermal coupled model of 18,650 LPF is established.

ARTICLE INFO

Keywords:
Heat generation
Nickel strip
Temperature rise
Lithium-ion battery

ABSTRACT

Thermal condition is crucial to the safety and performance of battery and battery pack. In this work, a two–dimensional, axisymmetric, electrochemical–thermal coupled model of 18,650 lithium–iron–phosphate battery is established and validated by our own experimental results. The model is used to investigate the effect of ambient temperature on battery performance and heat generation. The results show that the temperature rise in the battery increases with decreasing ambient temperature, which is mainly due to the increase in heat generated from Ohmic loss and polarization with decreased ambient temperature. While considering the welded structure, in which the cylindrical batteries are assembled into a battery pack, the effect of spot–welded nickel strip on battery performance under different discharge rates is experimentally studied at the ambient temperature of 298.15 K. It is found that the battery with the spot-welded nickel strip has a lower discharge plateau and a higher heat generation rate. The nickel strip has a greater impact on battery performance and temperature if the discharge C-rate increases.

1. Introduction

As a storage of electrical energy and transmitter, batteries play a vital role in the contemporary society. Lithium–ion batteries are widely used as power source in mobile phones, electric vehicles (EVs), and hybrid electric vehicles (HEVs), with the advantages of high energy density and high power [1,2]. Compared with lithium -manganese-oxide ($LiMn_2O_4$, LMO) and lithium-cobalt-oxide ($LiCoO_2$) batteries, the lithium–iron–phosphate (LPF) battery achieves better thermal stability, larger flat voltage plateau, and lower price; hence, it attracts the interest of the society more [3–5]. However, the heat behavior of the LPF battery has a certain impact on its safety and performance, unfortunately resulting in thermal runaway, which harms the safety of the entire vehicle. Hence, research on the thermal behavior of LPF battery is very meaningful [6–8].

Aiming for the thermal management of lithium batteries, an electrochemical –thermal coupled model of lithium battery with gradually improved calculation accuracy and efficiency has been developed [9–11]. Based on concentrated solution, porous electrode, and electrode dynamics theories, scholars have established several electrochemical models. At present, most electrochemical–thermal coupled models of lithium-ion batteries are established for LMO and $LiCoO_2$ batteries [12–14]. As the attention on LPF batteries increases, some scholars studied cylindrical LPF batteries. Most studies focused on the effect of the discharge rate on the thermal behavior of batteries [15–18]. Han et al. [19] proved that ambient temperature also has a significant effect on the thermal behavior and voltage of the LPF battery, but didn't analyze the heat generation of the LPF battery in detail.

Many factors affect battery heat generation. Currently, most research on battery tabs is focused on pouch cell batteries [20–23]. Bahiraei et al. [24,25] developed a thermoelectric coupling model of a three-dimensional lithium battery and analyzed the effects of thermal

* Corresponding author.
E-mail address: liuxl@me.ustb.edu.cn (X. Liu).

https://doi.org/10.1016/j.applthermaleng.2019.114648
Received 10 July 2019; Received in revised form 23 October 2019; Accepted 4 November 2019
Available online 05 November 2019
1359-4311/

Nomenclature

a_s	specific interfacial area, ($m^2\,m^{-3}$)
c	concentration of lithium ion at the elec-trode/electrolyte interface, ($mol\,m^{-3}$)
c_s	concentration of lithium ion in solid electrode, ($mol\,m^{-3}$)
c_e	concentration of lithium ion in elec-trolyte, ($mol\,m^{-3}$)
$c_{s,max}$	maximum solid Li + concentration for solid electrode ($mol\,m^{-3}$)
C_p	special heat capacity, ($J\,kg^{-1}\,K^{-1}$)
D_e	diffusion coefficient in electrolyte
D_s	diffusion coefficient of lithium ion in solid electrode particles, ($m^2\,s^{-1}$)
E_{eq}	open circuit voltage, (V)
F	Faraday's constant, ($C\,eq^{-1}$)
h	effective heat transfer coefficient, ($W\,m^{-2}\,K^{-1}$)
i_0	exchange current density, ($A\,m^{-1}$)
J^{Li}	transfer current resulted from insertion/ de-insertion of Li, ($A\,m^{-3}$)
k	electrochemical reaction rate constant, ($m\,s^{-1}$)
k_T	effective thermal conductivity of the active battery material, ($W\,m^{-1}\,K^{-1}$)
L	thickness of the difference layers of the cell, (m)
Q	heat generation rate, (W)
r	radium of the spherical particle, (m)
R	universal gas constant, ($J\,mol^{-1}\,K^{-1}$)
t	time, (s)
t_+^0	transfer number of lithium ion
T	absolute temperature, (K)
T_∞	ambient temperature, (K)

Greek symbols

α	charge transfer coefficients
σ	electric conductivity, ($S\,m^{-1}$)
ε	volume fraction of a phase
η	activation over-potentials of an electrode reaction, (V)
ϕ_l	electrolyte phase potential, (V)
ϕ_s	solid phase potential, (V)
ρ	effective density of the active battery material, ($kg\,m^{-3}$)
σ_{sb}	Stefan-Boltzmann constant, ($W\,m^{-2}\,K^{-4}$)
∇	gradient operator

Subscripts

l	electrolyte phase
n	negative electrode
o	initial value
p	positive electrode
i	different layer of active battery material
s	separator
∞	ambient

Superscripts

brug	Bruggeman coefficien
Li	lithium
ref	reference

Acronyms

CC	constant current
CV	constant voltage
EV	electric vehicle
HEV	hybrid electric vehicle
li-ion	lithium ion
LPF	lithium phosphate
PC	person computer
P2D	pseudo two dimensional
SOC	state of charge

contact resistance and SEI film on battery heat generation. Saxena et al. [26] studied the effects of internal current collector on heat generation, as well as the effects of burrs from welding on battery heat generation and safety. Saw et al. [27] simulated the effect of contact resistance on battery performance and on temperature distribution after battery discharge. For cylindrical batteries, parallel or series connection through the bus is necessary to assemble a battery pack, which must be connected to the external circuit at both ends. The bus is commonly spot-welded with welded nickel strips outside the electrode end of the cylindrical battery, which generates additional resistance [28–30]. The effect of the welded nickel strip on battery performance seems relatively small and few studies focused on it. However, for a battery pack, the effect of this structure on battery performance and thermal behavior can be amplified, which affects the temperature distribution and consistency of the entire battery pack. This effect need to be figured out, which is helpful for battery design optimization.

In the present study, a two-dimensional axisymmetric electrochemical–thermal coupled model was developed for 18,650 LPF battery. The developed model was validated through test results under different ambient temperatures. The effect of ambient temperature on the heat-generation mechanism of the battery was further analyzed. The thermal characteristics of cylindrical batteries with/without welded nickel strip was experimentally investigated to evaluate the effect of the welded structure on battery performance.

2. Model development

The single cell of LPF 18,650 cylindrical battery is shown in Fig. 1, in which the positive electrode is made from olivine-type lithium iron phosphate, the negative electrode is porous carbon LiC6, and the electrolyte is LiPF6 in EC: DEC 1: 1. The nominal voltage and capacity of the18650 LFP battery are 3.2 V and 1530 mAh, respectively. The battery was disassembled and the thicknesses of the battery electrode and diaphragm were measured using a spiral micrometer. Fig. 2 presents the disassembling process; Fig. 2(a) shows the removal of the Polyvinyl chloride (PVC) thermoplastic layer and positive cap, and Fig. 2(b) shows the removal of the battery can and illustrates how the

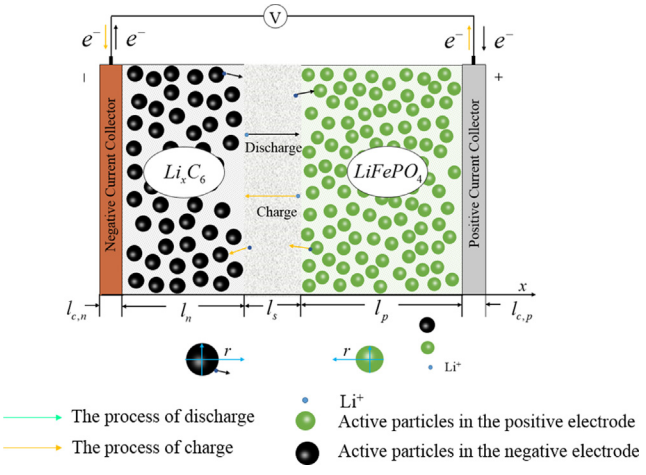

Fig. 1. Schematic of the 18,650 LPF battery.

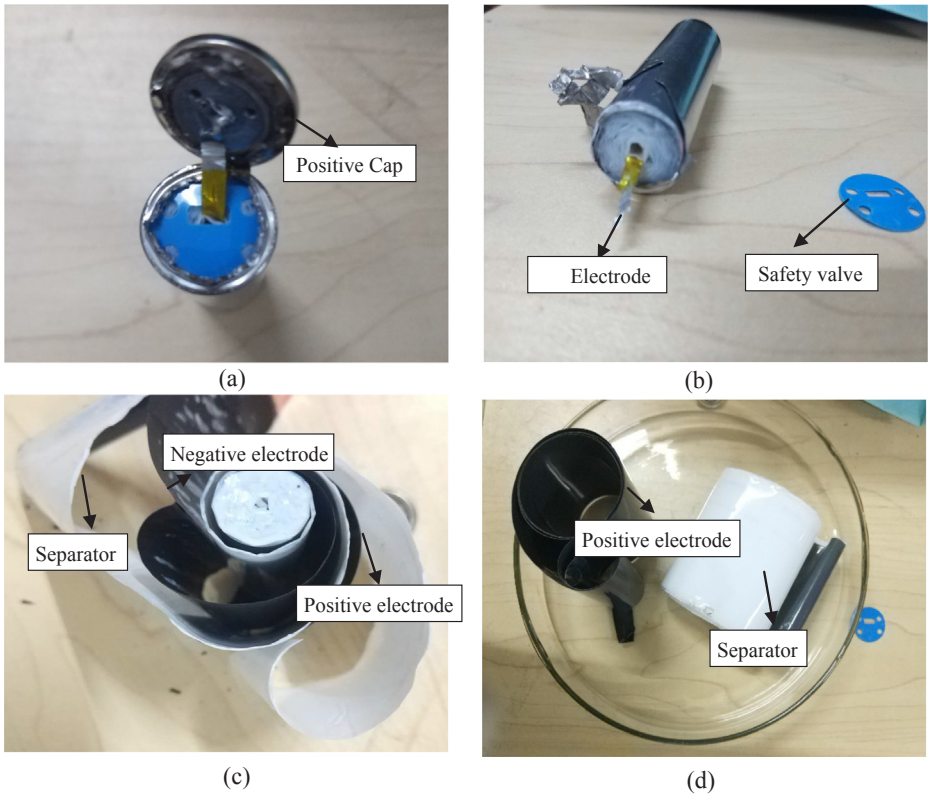

Fig. 2. Disassembled 18650LPF battery: (a) After stripping off the heat shrink wrapping and positive cap, (b) after stripping off the canister, (c) unroll the spiral wound, (d) disassembled positive electrode and separator.

battery is wound. Fig. 2(c) and (d) show the positive, negative, and diaphragm sections of the battery after disassembly.

The single cell is connected to the external circuit by positive and negative current collectors. When the battery is discharged, lithium ions are intercalated and de-intercalated at the positive and negative electrodes, respectively. The electrons generated and consumed by the electrode through a chemical reaction are transferred from the current collector to the external circuit to generate an external circuit current. During the charging process, lithium ions and electrons react in the battery in a manner opposite to the discharge process. The electrochemical reaction expression of the battery is given as follows [31]:

Negative electrode

$$LiC_6 \underset{Charge}{\overset{Discharge}{\rightleftharpoons}} Li_{1-x}C_6 + xLi^+ + e^- \tag{1}$$

Positive electrode

$$Li_{1-x}FePO_4 + xLi^+ + xe^- \underset{Charge}{\overset{Discharge}{\rightleftharpoons}} LiFeO_4 \tag{2}$$

A two-dimensional, axisymmetric, electrochemical-thermal coupled model is developed for the 18,650 LPF battery based on Newman's pseudo-two-dimensional electrochemical model (P2D) [32]. In the model, the concentration of ions inside the active particles is assumed as the function of the radial coordinate of the particle, and mass transfer between the adjacent two particles is neglected in the electrode. The model governing equations include mass and charge conservation equations which based on porous electrode and concentrated solution theories.

2.1. Mass conservation

Mass transfer in the solid phase involves the insertion and de-intercalation of lithium ions in active particles. In the P2D model, the Mass conservation in the solid phase is defined by Fick's second law in the spherical coordinate system, which is given by [32]:

$$\frac{\partial c_{s,i}}{\partial t} = D_{s,i}\frac{1}{r^2}\frac{\partial}{\partial r}\left(r^2\frac{\partial c_{s,i}}{\partial r}\right) \tag{3}$$

Boundary condition:

$$\begin{aligned} -D_{s,i}\frac{\partial c_{s,i}}{\partial r}|_{r=0} &= 0 \\ -D_{s,i}\frac{\partial c_{s,i}}{\partial r}|_{r=R_{s,i}} &= J_i^{Li} \end{aligned} \tag{4}$$

where $i = n, p, s$; $R_{s,i}$ is the radius of active particles in the positive and negative solid phases; $D_{s,i}$ is the diffusion coefficient of lithium in solid electrode particles; and $c_{s,i}$ is the concentration of lithium ion in the solid phase.

The electrolyte infiltrates the positive electrode, negative electrode, and the separator of the battery to carry out substance exchange between the positive and negative electrodes. The conservation of lithium ions in the electrolyte phase is derived from concentrated solution theory, which is given by [33]:

$$\frac{\partial(\varepsilon_i c_i)}{\partial t} = \frac{\partial}{\partial x}\left(D_i^{eff}\frac{\partial c_i}{\partial x}\right) + \frac{1-t_+^0}{F}J_i^{Li} - \left(\frac{i_t \nabla t_+}{F}\right) \tag{5}$$

Boundary condition:

$$-D_n^{eff}\frac{\partial c_n}{\partial x}|_{x=0} = -D_p^{eff}\frac{\partial c_p}{\partial x}|_{x=L} = 0 \tag{6}$$

where t_+^0 is the transfer number of lithium-ion that is dependent on the dissolution rate; it is a function of electrolyte concentration. D_i^{eff} is diffusion coefficient in electrolyte phase, which is given by:

$$D_i^{eff} = D_{e,i}\varepsilon_i^{brugg_i} \tag{7}$$

2.2. Charge conservation

The charge conservation in the solid phase is governed by Ohm's law [15,34]:

$$i_{s,i} = -\sigma_{eff,i}\frac{\partial \phi_{s,i}}{\partial x} \tag{8}$$

Boundary condition

$$\phi_s|_{x=0} = 0 \tag{9}$$

$$-\sigma_{eff,i}\frac{\partial \phi_{s,i}}{\partial x}\bigg|_{x=l_{cn}+l_n} = -\sigma_{eff,i}\frac{\partial \phi_{s,i}}{\partial x}\bigg|_{x=l_{cn}+l_n+l_s} = 0 \tag{10}$$

$$-\sigma_{eff,i}\frac{\partial \phi_{s,i}}{\partial x}\bigg|_{x=L} = \frac{I}{A} \tag{11}$$

where i = n and p, I is the current applied to the battery electrode, σ_{eff} is the effective conductivity of the solid phase, which is defined as

$$\sigma_{eff,i} = \sigma_i \varepsilon_s \tag{12}$$

The charge conservation in the electrolyte solution is given by [15,34]:

$$i_{e,i} = -k_{eff,i}\frac{\partial \phi_{e,i}}{\partial x} + \frac{2k_{eff,i}RT(1-t_+^0)}{F}\left(1+\frac{d\ln f_{\pm}}{d\ln c_i}\right)\frac{\partial \ln c_i}{\partial x} \tag{13}$$

Boundary condition

$$\frac{\partial \phi_{e,i}}{\partial x}\bigg|_{x=l_{cn}} = \frac{\partial \phi_{e,i}}{\partial x}\bigg|_{x=l_{cn}+l_n+l_s+l_p} = 0 \tag{14}$$

where i = n and p, $f_{\pm}$ is the molecular activity coefficient of electrolyte, $k_{eff,i}$ is the effective diffusional conductivity, which is defined by Burggeman relation

$$k_{eff,i} = k_i \varepsilon_i^{brug} \tag{15}$$

2.3. Electrochemical kinetics

The control equations of material conservation and charge conservation are combined by electrochemical kinetics according to Butler – Volmer equation and constitute a complete battery electrochemical control equation. The Butler – Volmer equation is given by [35,36]:

$$J_i^{Li} = a_{s,i} i_0 \left\{\exp\left(\frac{\alpha_a F}{RT}\eta_i\right) - \exp\left(\frac{\alpha_c F}{RT}\eta_i\right)\right\} \tag{16}$$

where i_0 is exchange current density, which is given by:

$$i_0 = k_i (c_{s,i,\max} - c_{s,i,surf})^{\alpha_a} c_{s,i,surf}^{\alpha_c} c_i^{\alpha_a} \tag{17}$$

where η_i is overpotential, which is defined as follows:

$$\eta_i = \phi_{s,i} - \phi_{l,i} - E_{eq,i} \tag{18}$$

where E_{eq} is the electrode equilibrium potential, which is a function of the state of charge and temperature of the battery electrode. Eq. (18) is expanded by the Taylor formula, and the first order approximation is given by

$$E_{eq,i} = E_{eq,ref,i} + (T - T_{ref})\frac{\partial E_{eq,i}}{\partial T} \tag{19}$$

2.4. Energy conservation equation

For a cylindrical battery, the energy conservation equation is given by [15]:

$$\rho C_p \frac{\partial T}{\partial t} = \nabla \cdot k_T \nabla T + Q \tag{20}$$

and the boundary condition is given by Newton's law of cooling and Kirchhoff's law as follows:

$$\left(-k_T\frac{\partial T}{\partial x}\right)_{x=L} = h(T - T_a) + E\sigma_{SBc}(T^4 - T_a^4) \tag{21}$$

where T_a is the ambient temperature, σ_{SBc} is Stenfan-Boltzman constant.

The battery comprises three parts of internal heat source, which are given by [36]:

Polarization heat:

$$Q_{reac,i} = J_i^{Li}\eta_i \tag{22}$$

Reaction heat:

$$Q_{rea,i} = J_i^{Li} T\left(\frac{\partial E_{eq,i}}{\partial T}\right) \tag{23}$$

Ohmic heat:

$$Q_{ohm,i} = \sigma_{eff,i}\left(\frac{\partial \phi_{s,i}}{\partial x}\right)^2 + k_{eff,i}\left(\frac{\partial \phi_{l,i}}{\partial x}\right)^2 + \frac{2k_{eff,i}RT}{T}(1-t_+^0)\frac{\partial(\ln c_i)}{\partial x}\frac{\partial \phi_{l,i}}{\partial x} \tag{24}$$

The total battery heat is calculated using Eq. (16) as follows:

$$Q_{tot,i} = Q_{rev,i} + Q_{rea,i} + Q_{ohm,i} \tag{25}$$

In this study, the thermal conductivity of the battery is defined as anisotropy to study the distribution of battery temperature according to the characteristics of the stacked battery. The characteristics of the cylindrical battery show that the thermal conductivity in the circumferential direction is uniform. Hence, in this study, thermal conductivity is studied in the axial and radial directions. The thermal conductivity in two directions is defined by

$$k_{T,r} = \frac{\sum L_i}{\sum {}^{Li}/_{k_{T,i}}},\ k_{T,ang} = \frac{\sum L_i k_{T,i}}{\sum L_i} \tag{26}$$

2.5. Model coupling

The electrochemical model is established by the governing equation, and the heat transfer model is established by the energy conservation equation coupled with the battery parameters, which are defined by temperature. For example, the dependence of diffusion coefficient and ionic conductivity on temperature is expressed by the Arrhenius formula [37]:

$$D_{s,i} = D_{s,ref,i}\exp\left[-\frac{E_{d,i}}{R}\left(\frac{1}{T}-\frac{1}{T_{ref}}\right)\right],\ k_{l,i} = k_{l,ref,i}\exp\left[-\frac{E_{r,i}}{R}\left(\frac{1}{T}-\frac{1}{T_{ref}}\right)\right] \tag{27}$$

2.6. Numerical solution method

The multi-physics coupling calculation software COMSOL Multiphysics 5.3a based on the finite element method is used to solve the two-dimensional, axisymmetric, electrochemical–thermal coupled model of 18,650 lithium–iron–pho-sphate battery. The solution requires about 300 s on a 3.5 GHz, Ryzen 5 PRO personal computer. Table 1 gives the experimentally measured battery physical dimensions and the physical properties of the battery material. These data are used to solve the battery model established in this paper. Table 2 presents the chemical parameters of the 1.53 Ah LPF battery. The parameters are selected according to the same battery material and state of charge in the literature.

3. Experimental

A schematic and photograph of the experimental setup are

Table 1
Thermal and electrical parameters for LPF cell.

Parameter	Negative	Separator	Positive
Length, (μm)*	50	25	75
Current collector thickness, (mm)*	20	_	10
Thermal conductivity, ($Wvm^{-1}K^{-1}$) [27]	0.2	0.334	1.04
Current collector thermal conductivity, ($W m^{-1}K^{-1}$) [27]	170	_	398
Density, ($kg m^{-3}$) [27]	1347	1009	3600
Current collector density, [$kg m^{-3}$] [27]	8933	_	2770
Heat capacity, ($J kg^{-1}K^{-1}$)] [27]	1437	1978	750
Current collector heat capacity, ($J kg^{-1}K^{-1}$)] [27]	385	_	875
Thickness of battery canister, $(mm)^{-}$	0.5	_	_
Battery radius, $(mm)^{-}$	9	_	_
Battery height, $(mm)^{-}$	65	_	_
Mandrel radius, $(mm)^{-}$	1.5	_	_
Heat Transfer coefficient, ($W m^{-2}K^{-1}$)	5	_	_

Table 2
Model input parameters for 1.53Ah LPF cell.

Parameter	Negative	Separator	Positive
Particle radius, r (μm) [15]	6.5	_	0.5
Electrolyte phase volume fraction, ε_l [15]	0.363	0.724	0.417
Electrode phase volume fraction, ε_s [15]	0.585	_	0.513
Initial electrolyte concentration $c_{l,0}$, ($mol m^{-3}$) [15]	1200	1200	1200
Maximum Li concentration in solid $c_{s,max}$, ($mol m^{-3}$) [15]	26,390	_	22,800
Charge transfer coefficient α_c, α_a [3]	0.5, 0.5	_	0.5, 0.5
Electric conductivityσ, ($S m^{-1}$) [3]	100	_	3.8
Bruggeman coefficient for tortuosity [3]	2.4	1.5	1.8

presented in Fig. 3. The test bench system consists of two computers, Maccor multifunction series 4000 automated test system (MMS4000, Maccor. Inc), Maccor multitemperature benchtop mount temperature chamber (MTC, Maccor. Inc), Agilent 34970A data acquisition system (DAS, Agilent Technologies Co. Ltd), FLIR T420 thermal imaging camera, and T-type thermocouples. The MMS4000 is used to control the charge/discharge process with the operating voltage and current ranged from 0 V to 180 V and 0 A to 2000 A, respectively. PC1 is used to set the battery charge and discharge process and record the battery operating parameters, such as voltage and capacity. The MTC provides a constant operating temperature for the 18,650 LPF battery to test the performance of the battery at different ambient temperatures. DAS connecting to PC2 is used for recording the temperature information collected by the array of T-type thermocouples settled on the external surface of the battery. FLIR T420 is used to measure the temperature distribution of the battery surface after discharging, and the obtained data can be used to qualitatively analyze the distribution of the surface temperature of the battery [38,39].

The temperature distribution of the cylindrical battery exhibits symmetry characteristics. Hence, thermocouples are placed on one side of the battery. The other side of the battery is used to measure the surface temperature distribution by using the thermal imager. The schematic and photographs of the thermocouple arrangement are shown in Fig. 4(a) and (b).

In this study, the first set of experiments are performed to study the effect of ambient temperature on battery performance. And the second set of experiments are performed to investigate the effect of tabs on the performance of the battery which welded on the positive and negative electrodes. In the first experiment, the battery is tested at a discharge rate of 1C at ambient temperatures of 288.15, 298.15, and 308.15 K. The C-rate is defined as the ratio of the charge and discharge current to its nominal capacity

$$C_{rate} = \frac{I}{Q_c} \tag{28}$$

where C_{rate} is charge/discharge rate, I is charge or discharge current, and Q_c is nominal capacity. The cut-off voltage for constant current discharging is set to 2 V and for constant charging current is 3.65 V. The battery is placed at room temperature for 4 h, and the charging process is carried out by constant-current and constant voltage (CC-CV) charging method. First, the battery is charged to a cut-off voltage of 3.65 V at a charging rate of 0.5C, as specified by the manufacturer, and then charged to a cut-off current of 0.02C with a constant voltage of 3.65 V to ensure that it is fully charged. After charging, it is then placed in the temperature-control chamber at the operating temperature for 4 h to ensure the stabilization of the battery chemistry and thermal equilibrium with the surrounded temperature. Finally, it is discharged to the cut-off voltage at 1C discharge rate.

In the second experiment, the test object is an 18,650 LPF battery with electrode spot-welded tabs. The purpose of this experiment is to test the effect of electrode spot-welded tabs on the battery performance at different discharge rates under room temperature. Laser spot welding is performed, and the resulting joint is shown in Fig. 5. The battery with the spot-welded tabs is placed in an environmental chamber at 298.15 K, and discharge tests are performed at rates of 1C, 2C, and 3C. The tests are conducted for a battery without the spot-welded tabs under the same operating conditions for comparison. Thermal images are captured at the end of battery discharge with the FLIR T420 thermal camera, whose measuring temperature range is set from 253.15 K to 393.15 K.

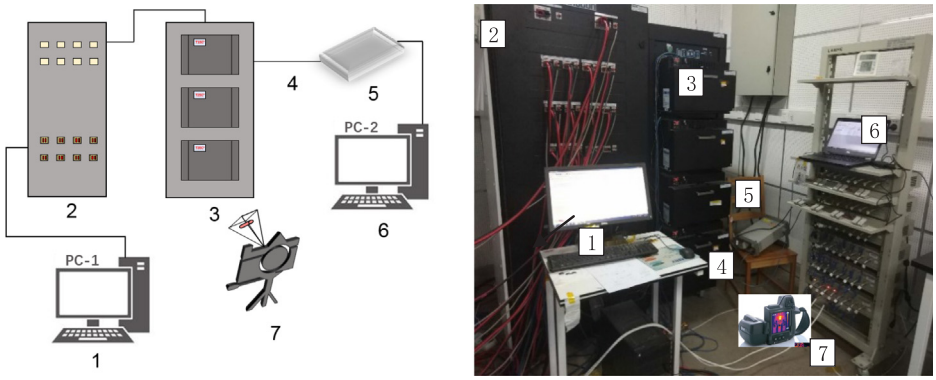

***(a)** Schematic of battery test bench;* ***(b)** 18650LPF battery test bench*

Fig. 3. Battery test bench, 1: PC1 for charge/discharge; 2: Maccor multifunction series 4000 automated test system; 3: temperature chamber; 4: T-type thermocouples; 5: Data acquisition system; 6: PC2 for temperature measurement; 7: FLIR T420 thermal imaging camera.

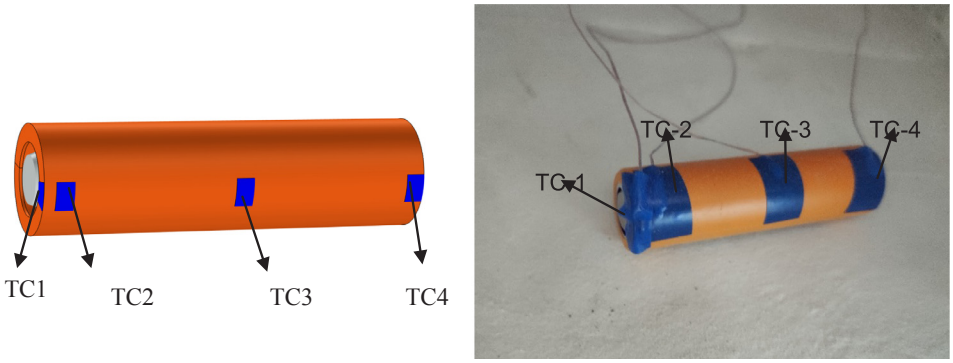

Fig. 4. (a) Schematic of arranged thermocouples. **(b)** Arranged thermocouples.

4. Result and discussion

4.1. Model validation

The discharge tests and corresponding simulations are conducted for the above mentioned 18,650 LPF battery at the rate of 1C while changing the ambient temperature. The results of voltage change and surface temperature rise are shown in Fig. 6, which compares the simulation and experimental results. It is found that the model prediction agrees well with experiments. The specific comparison between the simulation results and the experimental results is represented by relative error which calculated by MATLAB software. The relative errors of voltage are 0.65%, 0.46%, and 0.94% at different temperatures of 288.15, 298.15, and 308.15 K, respectively. The relative errors of battery temperature rise are 4.39%, 5.74%, and 8.46%.

It is found that the model prediction agrees well with the test results. The voltage discrepancy between the simulation and tests, i.e. relative error recalculated by MATLAB software, is 0.65–0.95%, while the temperature discrepancy is 4.2–8.5%. After discharging, the average values of the surface temperature increase are 8.8 K, 5.4 K, and 3.2 K, which are at the ambient temperatures of 288.15 K, 298.15 K, and 308.15 K, respectively.

4.2. Heat effect of the LPF battery

Fig. 7 shows heat generation rates in the battery during discharging. In general, the curves of the heat generation rates are similar in shape for tests at different temperatures. At the beginning of discharge, total heat generation rate increases sharply, then cuts down gradually, and again grows quickly at the end of discharge, as shown in Fig. 8a. In the initial stage of discharge, the battery temperature is identical to ambient. The electrical resistance from ion migration and electromigration is higher at a lower temperature, thus the relevant Ohmic heat generation rate grows fast in the beginning of discharge, especially at lower ambient temperature, as displayed in Fig. 7c. The electrical resistance drops with temperature rise during discharge, and the Ohmic heat generation rate decreases gradually. Nonetheless, the reaction heat generation rate is negative during most time of discharge, which shows an endothermic effect due to the intrinsic nature of the electrode material. While at the end of discharge, it grows rapidly and becomes positive, which shows exothermic effect due to the side reaction of discharge. Note it is found that the ambient temperature has a negligible effect on the reaction heat generation rate. However, the heat generation rate from polarization is remarkably relevant to the ambient temperature. Like Ohmic heat effect, the polarization heat increases while lowering the ambient temperature. At the final stage of discharge, the increase in heat generated from polarization and reaction leads to a rapid increase in the total heat generation rate and external surface temperature of the battery.

Furthermore, the proportions of the different types of heat generation rate to the total at the end of discharge are calculated and compared, as shown in Fig. 8. It shows the heat generation due to different mechanisms is varied at different regions, which are both affected by ambient temperature. In the final stage of discharge, the Ohmic heat accounts for the largest proportion, especially at lower ambient temperature due to higher electrical resistance. There is no apparent tendency of the heat-generated proportion at different temperature in the three domains, i.e. the positive electrode, separator, and negative electrode, with each proportion ranged from 15% to 50%. In the positive electrode, the proportion of heat generated from Ohmic thermal effect and polarization increases with decreasing the ambient temperature, with the proportion of each type ranged from 19% to 45%. Whereas the proportion of reaction heat cuts down with decreasing the ambient temperature, although the reaction heat generation rate grows with that, as seen from Fig. 8b. In the negative electrode, the reaction heat accounts for more than 78% of total heat generation, while Ohmic heat and polarization heat in turn. Also, the proportion of reaction heat reduces with decreasing the ambient temperature.

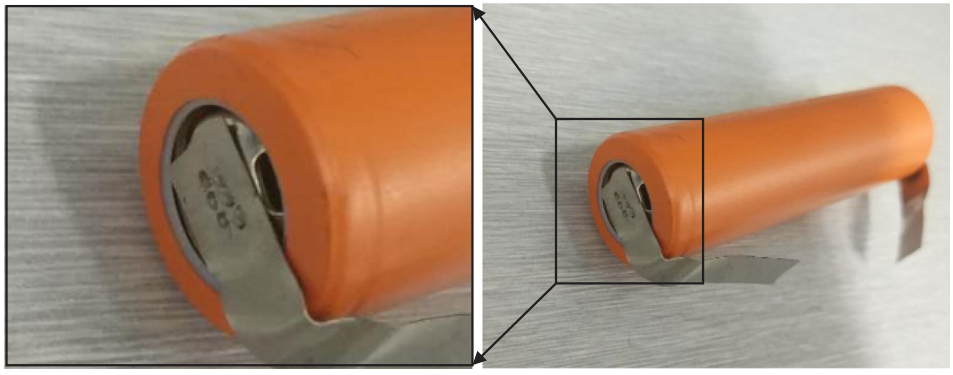

Fig. 5. Battery with spot-welded tabs.

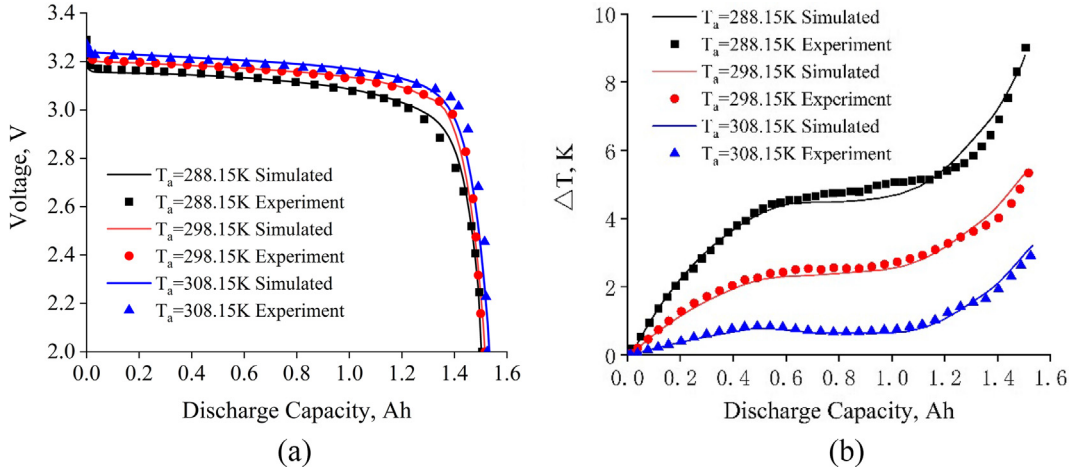

Fig. 6. Experimental and simulation results (a) cell potential, (b) temperature.

4.3. Effect of the electrode spot-welded tabs

For cylindrical battery pack, solder joints are formed when the nickel strip is spot welded onto one end of the battery. The solder joints create additional resistance and degrade battery performance. The discharge tests are conducted for 18,650 LPF batteries with and without spot-welded nickel tape under the identical operating conditions for comparison. The effects of ambient temperature and discharge rate on battery performance are also investigated.

Fig. 9 shows the discharge voltage and temperature rise of the battery with/without spot-welded nickel strips at different rates at the ambient temperature of 298.15 K. The relative uncertainty of the measured voltage is less than 1.8%. The voltage plateau of the battery with spot-welded tabs drops by 0.024 V, 0.026 V and 0.032 V, as compared with that without spot-welded tabs at three discharge rates of 1C, 2C, and 3C, respectively. The corresponding maximum temperature-

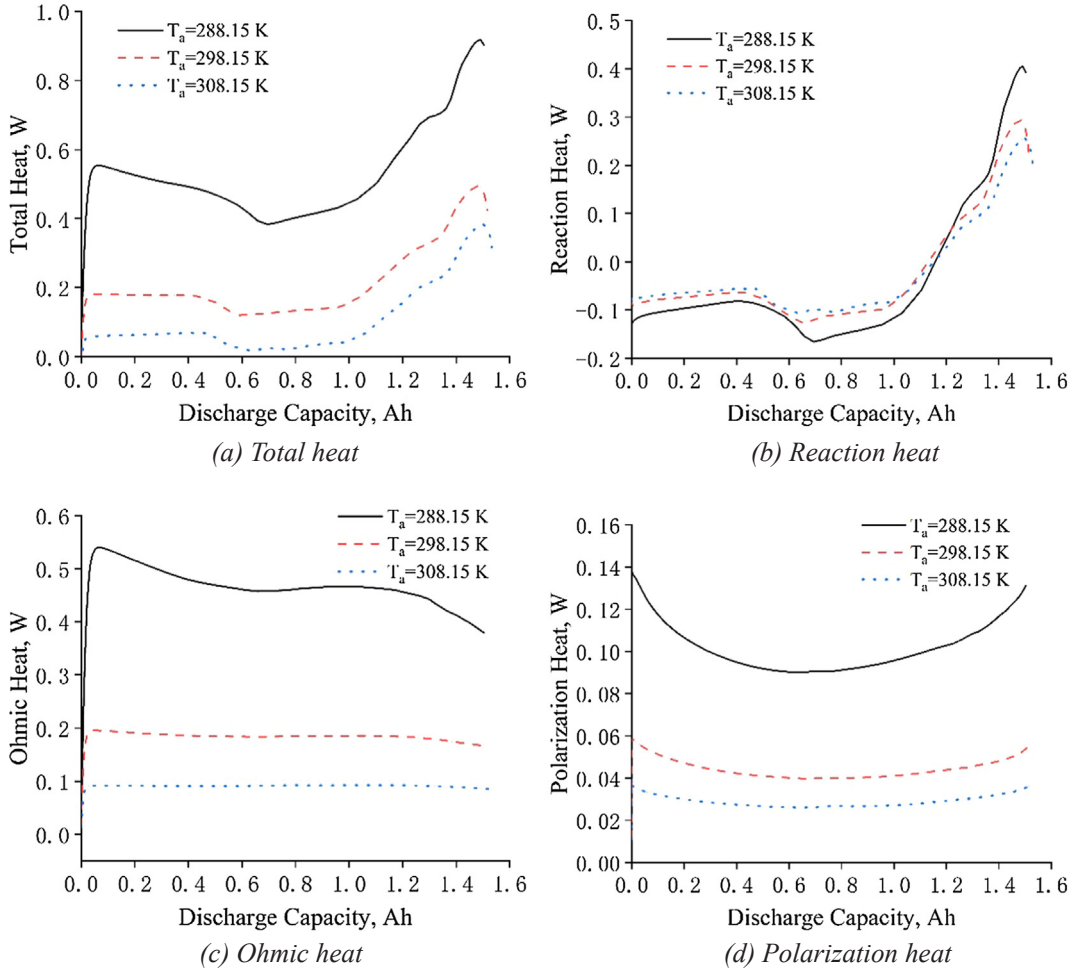

Fig. 7. Cell heat generated under different ambient temperatures of 288.15, 298.15 and 308.15 K.

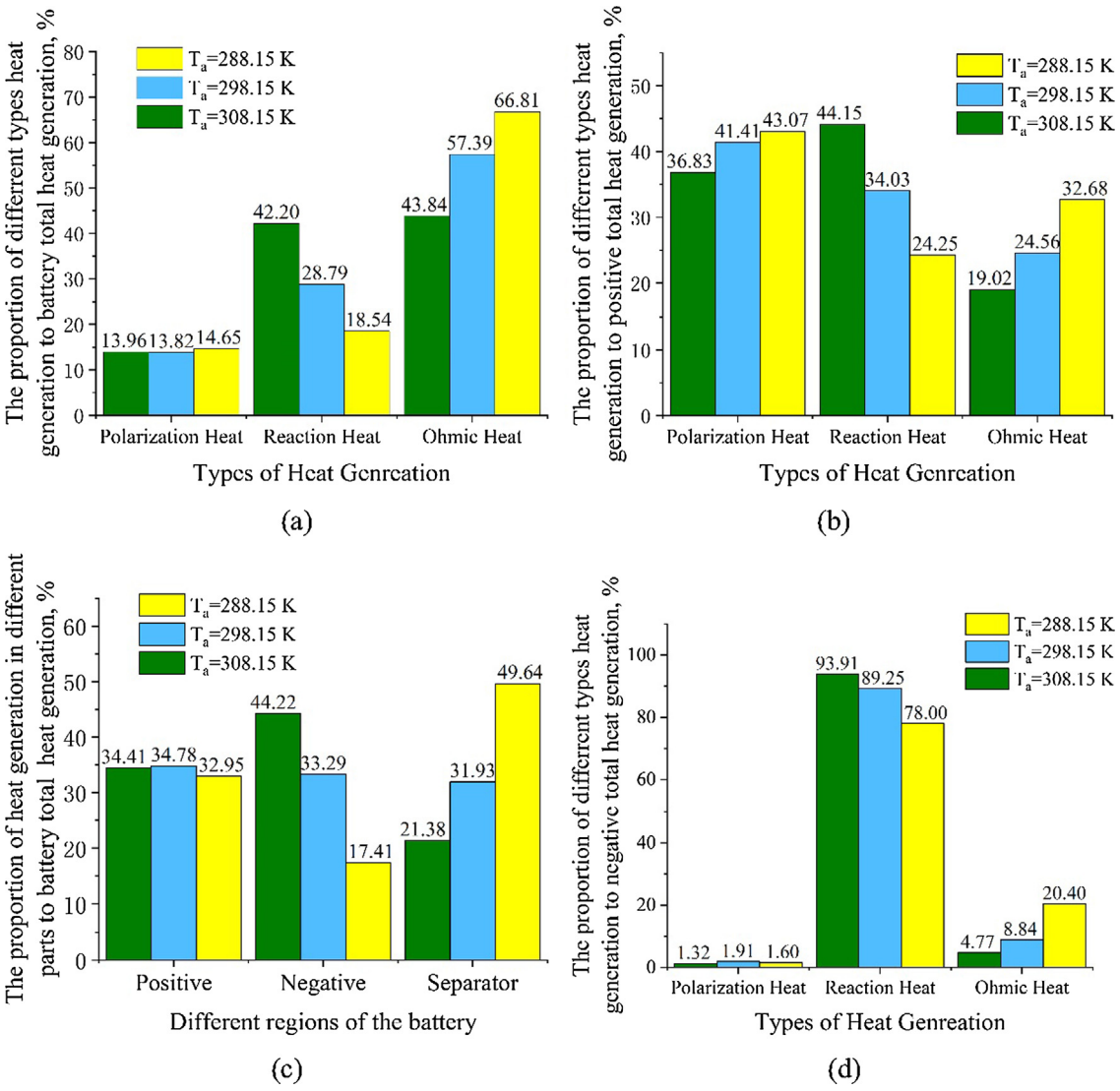

Fig. 8. Proportion of each part of heat generation at different ambient temperatures.

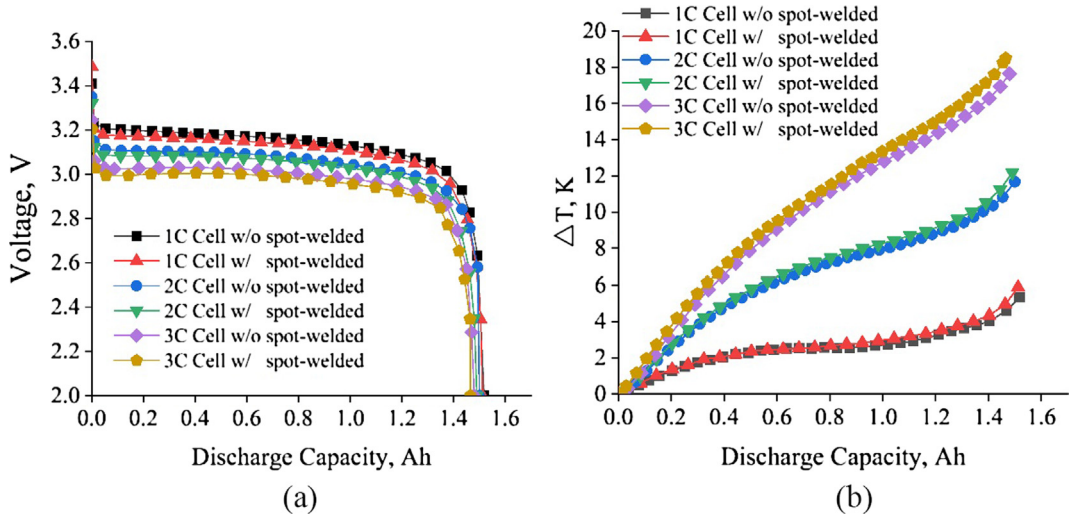

Fig. 9. Tested results of battery with/without tabs (a) cell potential, (b) temperature.

rise values on the surface of the spot-welded nickel strip are 0.6 K, 0.8 K, and 1.2 K, respectively. For the battery with the spot-welded nickel strip, a solder joint is formed at the junction of the electrode and nickel strip, which results in additional contact resistance. During the charge/discharge process, the battery solder joint will be heated due to the extra Joule thermal effect, which in turn raises the external surface temperature of battery. It is also found that the effect of spot-welded nickel strips increases with the discharge rate increasing.

Fig. 10 shows the thermal images of the external surface of batteries with/without spot-welded nickel strips at the end of the discharge. The highest temperature is marked with the white boxes, and the spot-welded area is marked with black boxes. As seen from Fig. 10(a) and (b), the surface temperature rise of the battery with welded tab is slightly higher than that without tabs at the discharge rate of 1C. While the discharge rate increases to 2C and 3C, the surface temperature of the battery with nickel strip increases remarkably, especially adjacent to the solder joint. The temperature difference between the batteries with and without nickel strip achieves the maximum of 2.5 K at 3C discharge rate. It seems reasonable because the heat generation rate is a quadratic function of discharge current. The thermal images demonstrates again that the spot-welded nickel strips have a greater effect on battery performance at a higher discharge rate.

5. Conclusion

In this work, a two-dimensional, axisymmetric, electrochemical-thermal coupled model is developed for 18,650 lithium–iron–phosphate battery. The battery discharge tests are conducted at different rates and temperatures so as to investigate the effects of ambient temperature and spot-welded nickel strip on battery performance. The results show that the battery surface temperature rise increases when the ambient temperature decreases, which is mainly due to the higher generation rate from Ohmic thermal effect and polarization at lower temperature. Meanwhile the ambient temperature has a negligible effect on the reaction heat generation rate. It is found that the battery with spot-welded tabs has a lower voltage platform and higher temperature increase compared with that without spot-welded tabs. The maximum values of voltage drop and temperature rise at a discharge rate of 3C reach 0.032 V and 2.5 K, respectively. The effect of spot-welded nickel strip on the battery performance becomes more significant at a higher discharge rate. It can be expected that the welded strips affect the thermal performance of the battery pack, which deserves further

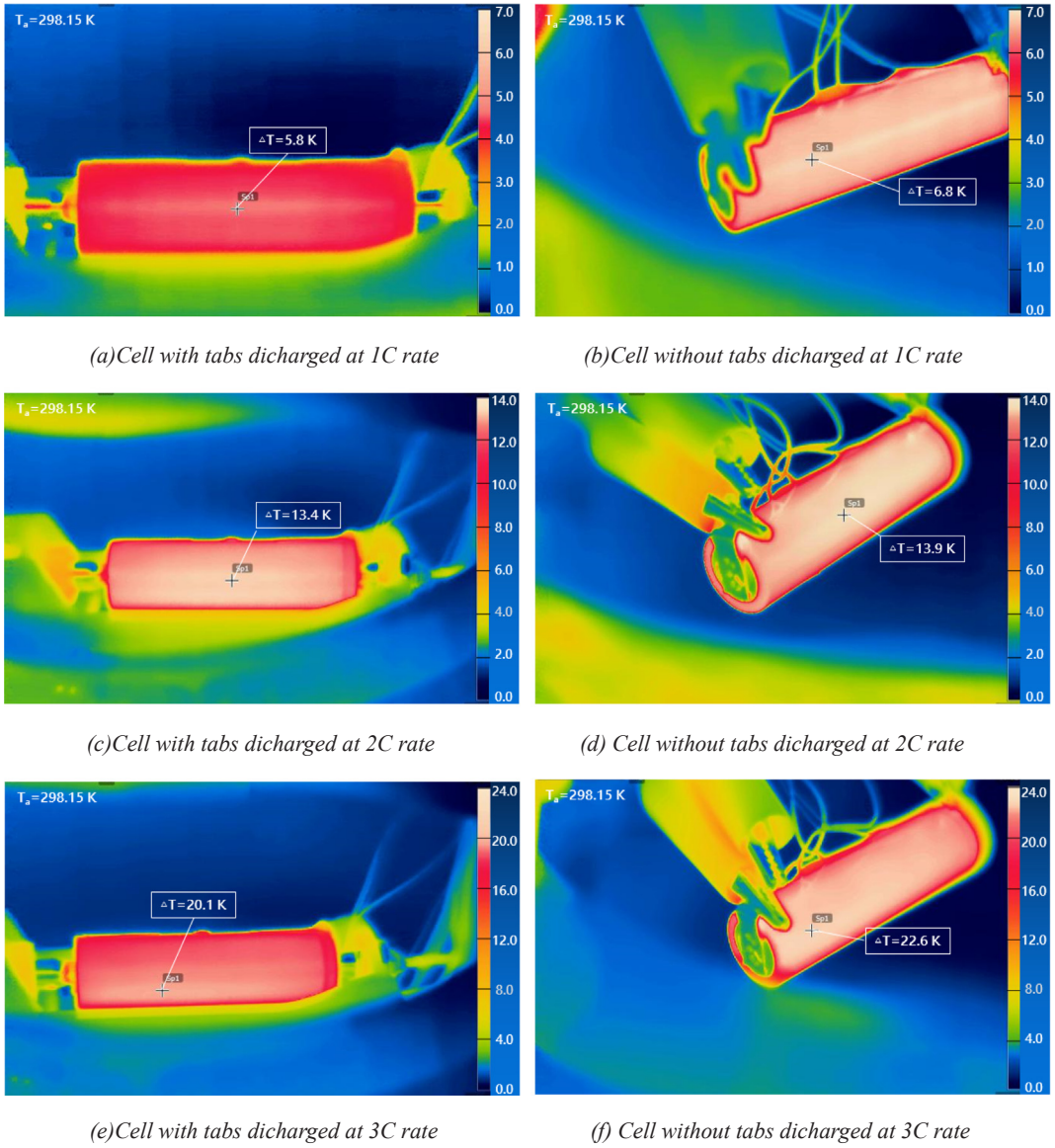

(a)Cell with tabs dicharged at 1C rate *(b)Cell without tabs dicharged at 1C rate*

(c)Cell with tabs dicharged at 2C rate *(d) Cell without tabs dicharged at 2C rate*

(e)Cell with tabs dicharged at 3C rate *(f) Cell without tabs dicharged at 3C rate*

Fig. 10. Thermal image of the cell with/without tabs at different discharge rates.

attention.

Declaration of Competing Interest

We declare that we have no financial and personal relationships with other people or organizations that can inappropriately influence our work, there is no professional or other personal interest of any nature or kind in any product, service and/or company that could be construed as influencing the position presented in, or the review of, the manuscript entitled, “Experimental and simulation study on thermal characteristics of 18650 lithium–iron–phosphate battery with and without spot–welding tabs”.

Acknowledgments

This work was supported by the National Natural Science Foundation of China (No. 51676013). The authors thank Prof. Jianbo Zhang from Tsinghua University for his laboratory providing some sets for batteries tested. L. Liu would like to acknowledge the support from the National Science Foundation under Grant Number 1840732. In the meanwhile, L. Liu would like to thank the support from KS NASA EPSCoR program and KU General Research Fund.

Appendix A. Supplementary material

Supplementary data to this article can be found online at https://doi.org/10.1016/j.applthermaleng.2019.114648.

References

[1] J.M. Tarascon, M. Armand, Issues and challenges facing rechargeable lithium batteries, Nature 414 (2001) 171–179.
[2] R.V. Kumar, T. Sarakonsri, High Energy Density Lithium Batteries: Materials, Engineering, Wiley-VCH, Applications. High Energy Density Lithium Batteries, 2010.
[3] L.X. Yuan, Z.H. Wang, Development and challenges of LiFePO4cathode material for lithium-ion batteries, Energy Environ. Sci. 4 (2011) 269–284.
[4] X.K. Zhang, X.H. Chang, Y.D. Shen, Y. Xiang, Electrochemical-electrical-thermal modeling of a pouch-type lithium ion battery: an application to optimize temperature distribution, J. Storage Mater. 11 (2017) 249–257.
[5] R. Kantharaj, A.M. Marconnet, Heat generation and thermal transport in lithium-ion batteries: a scale-bridging perspective, Nanoscale Microscale Thermophys. Eng. 23 (2019) 128–156.
[6] Y.W. Tang, L.J. Wu, W.F. Wei, D.Q. Wen, Q.W. Guo, W.C. Liang, L. Xiao, Study of the thermal properties during the cyclic process of lithium ion power batteries using the electrochemical-thermal coupling model, Appl. Therm. Eng. 137 (2018) 11–22.
[7] S. Abada, M. Petit, A. Lecocq, G. Marlair, V.S. Moynot, F. Huet, Combined experimental and modeling approaches of the thermal runaway of fresh and aged lithium-ion batteries, J. Power Sources 399 (2018) 264–273.
[8] S.Q. Zheng, L. Wang, X.N. Feng, X.M. He, Probing the heat sources during thermal runaway process by thermal analysis of different battery chemistries, J. Power Sources 378 (2018) 527–536.
[9] P.F. Salazar, S. Kumar, B.A. Cola, Design and optimization of thermo-electrochemical cells, J. Appl. Electrochem. 44 (2013) 325–336.
[10] S.U. Kim, P. Albertus, D. Cook, C.W. Monroe, J. Christensen, Thermoelectrochemical simulations of performance and abuse in 50-Ah automotive cells, J. Power Sources 268 (2014) 625–633.
[11] C. Kupper, W.G. Bessler, Multi-scale thermo-electrochemical modeling of performance and aging of a LiFePO4/Graphite Lithium-ion cell, J. Electrochem. Soc. 164 (2017) A304–A320.
[12] N. Baba, H. Yoshida, M. Nagaoka, C. Okuda, S. Kawauchi, Numerical simulation of thermal behavior of lithium-ion secondary batteries using the enhanced single particle model, J. Power Sources 252 (2014) 214–228.
[13] S. Panchal, I. Dincer, M.A. Chaab, R. Fraser, M. Fowler, Experimental and theoretical investigation of temperature distributions in a prismatic lithium-ion battery, Int. J. Therm. Sci. 99 (2016) 204–212.
[14] M. Farag, H. Sweity, M. Fleckenstein, S. Habibi, Combined electrochemical, heat generation, and thermal model for large prismatic lithium-ion batteries in real-time applications, J. Power Sources 360 (2017) 618–633.
[15] N.X. Yang, X.W. Zhang, G.J. Li, D. Hua, Assessment of the forced air-cooling performance for cylindrical lithium-ion battery packs: a comparative analysis between aligned and staggered cell arrangements, Appl. Therm. Eng. 80 (2015) 55–65.
[16] S. Panchal, M. Mathew, R. Fraser, M. Fowler, Electrochemical thermal modeling and experimental measurements of 18650 cylindrical lithium-ion battery during discharge cycle for an EV, Appl. Therm. Eng. 135 (2018) 123–132.
[17] J. Chiew, C.S. Chin, W.D. Toh, Z. Gao, J. Jia, C.Z. Zhang, A pseudo three-dimensional electrochemical-thermal model of a cylindrical LiFePO4/graphite battery, Appl. Therm. Eng. 147 (2019) 450–463.
[18] S.X. Wang, K.X. Li, Y. Tian, J.Y. Wang, Y.K. Wu, S. Ji, An experimental and numerical examination on the thermal inertia of a cylindrical lithium-ion power battery, Appl. Therm. Eng. 154 (2019) 676–685.
[19] X.F. Han, Y.X. Huang, H.X. Lai, Electrochemical-thermal coupled investigation of lithium iron phosphate cell performances under air-cooled conditions, Appl. Therm. Eng. 147 (2019) 908–916.
[20] U.S. Kim, C.B. Shin, C.S. Kim, Effect of electrode configuration on the thermal behavior of a lithium-polymer battery, J. Power Sources 180 (2008) 909–916.
[21] S. Goutam, A. Nikolian, J. Jaguemont, J. Smekens, N. Omar, P.V.D. Bossche, J.V. Mierlo, Three-dimensional electro-thermal model of li-ion pouch cell: analysis and comparison of cell design factors and model assumptions, Appl. Therm. Eng. 126 (2017) 796–808.
[22] J. Yi, U.S. Kim, C.B. Shin, T. Han, S. Park, Three-dimensional thermal modeling of a Lithium-ion battery considering the combined effects of the electrical and thermal contact resistances between current collecting tab and lead wire, J. Electrochem. Soc. 160 (2013) A437–A443.
[23] W.X. Mei, H.D. Chen, J.H. Sun, Q.S. Wang, Numerical study on tab dimension optimization of lithium-ion battery from the thermal safety perspective, Appl. Therm. Eng. 142 (2018) 148–165.
[24] F. Bahiraei, M. Ghalkhani, A. Fartaj, G.A. Nazri, A pseudo 3D electrochemical-thermal modeling and analysis of a lithium-ion battery for electric vehicle thermal management applications, Appl. Therm. Eng. 125 (2017) 904–918.
[25] M. Ghalkhani, F. Bahiraei, G.A. Nazri, M. Saif, Electrochemical-thermal model of pouch-type lithium-ion batteries, Electrochim. Acta 247 (2017) 569–587.
[26] X.Y. Yao, S. Saxena, L. Su, M.G. Pecht, The explosive nature of tab burrs in Li-ion batteries, IEEE Access (2019) 45978–45982.
[27] L.H. Saw, Y.H. Ye, A.A.O. Tay, Electrochemical–thermal analysis of 18650 lithium iron phosphate cell, Energy Convers. Manage. 75 (2013) 162–174.
[28] L.H. Saw, Y. Ye, A.A.O. Tay, Electro-thermal analysis and integration issues of lithium ion battery for electric vehicles, Appl. Energy 131 (2014) 97–107.
[29] L.H. Saw, Y.H. Ye, A.A.O. Tay, W.T. Chong, S.H. Kuan, M.C. Yew, Computational fluid dynamic and thermal analysis of Lithium-ion battery pack with air cooling, Appl. Energy 177 (2016) 783–792.
[30] Y.F. Lv, X.Q. Yang, G.Q. Zhang, X.X. Li, Experimental research on the effective heating strategies for a phase change material based power battery module, Int. J. Heat Mass Transf. 128 (2019) 392–400.
[31] F. Jiang, P. Peng, Y. Sun, Thermal analyses of LiFePO 4 /graphite battery discharge processes, J. Power Sources 243 (2013) 181–194.
[32] V. Ramadesigan, P.W.C. Northrop, S. De, S. Santhanagopalan, R.D. Braatz, V.R. Subramanian, Modeling and simulation of lithium-ion batteries from a systems engineering perspective, J. Electrochem. Soc. 159 (2012) R31–R45.
[33] S.L. Genong Li, Physics-based CFD simulation of lithium-ion battery under the FUDS driving cycle, ECS Trans. 64 (2015) 1–14.
[34] T.F. Fuller, M. Doyle, J. Newman, Simulation and optimization of the dual lithium ion insertion cell, Electorchem. Sci. Technol. 141 (1994) 1–10.
[35] K.A. Smith, C.D. Rahn, C.Y. Wang, Control oriented 1D electrochemical model of lithium ion battery, Energy Convers. Manage. 48 (2007) 2565–2578.
[36] L. Cai, R.E. White, Mathematical modeling of a lithium ion battery with thermal effects in COMSOL Inc., Multiphysics (MP) software, J. Power Sources 196 (2011) 5985–5989.
[37] L.O. Valøen, J.N. Reimers, Transport properties of LiPF6-based Li-ion battery electrolytes, J. Electrochem. Soc. 152 (2005) A882–A891.
[38] J. Zhao, Z. Rao, Y. Huo, Thermal management of cylindrical power battery module for extending the life of new energy electric vehicles, Appl. Therm. Eng. 80 (2015) 33–43.
[39] S. Panchal, I. Dincer, R. Fraser, M. Fowler, Experimental and simulated temperature variations in a LiFePO4-20Ah battery during discharge process, Appl. Energy 180 (2016) 504–515.